JOURNAL OF GEOPHYSICAL RESEARCH, VOL. 113, C05008, doi:10.1029/2007JC004343, 2008

Formation of undular bores and solitary waves in the Strait of Malacca caused by the 26 December 2004 Indian Ocean tsunami

J. Grue,[1] E. N. Pelinovsky,[2] D. Fructus,[1] T. Talipova,[2] and C. Kharif[3]

Received 16 May 2007; revised 17 October 2007; accepted 28 December 2007; published 7 May 2008.

[1] Deformation of the Indian Ocean tsunami moving into the shallow Strait of Malacca and formation of undular bores and solitary waves in the strait are simulated in a model study using the fully nonlinear dispersive method (FNDM) and the Korteweg-deVries (KdV) equation. Two different versions of the incoming wave are studied where the waveshape is the same but the amplitude is varied: full amplitude and half amplitude. While moving across three shallow bottom ridges, the back face of the leading depression wave steepens until the wave slope reaches a level of 0.0036–0.0038, when short waves form, resembling an undular bore for both full and half amplitude. The group of short waves has very small amplitude in the beginning, behaving like a linear dispersive wave train, the front moving with the shallow water speed and the tail moving with the linear group velocity. Energy transfer from long to short modes is similar for the two input waves, indicating the fundamental role of the bottom topography to the formation of short waves. The dominant period becomes about 20 s in both cases. The train of short waves, emerging earlier for the larger input wave than for the smaller one, eventually develops into a sequence of rank-ordered solitary waves moving faster than the leading depression wave and resembles a fission of the mother wave. The KdV equation has limited capacity in resolving dispersion compared to FNDM.

Citation: Grue, J., E. N. Pelinovsky, D. Fructus, T. Talipova, and C. Kharif (2008), Formation of undular bores and solitary waves in the Strait of Malacca caused by the 26 December 2004 Indian Ocean tsunami, *J. Geophys. Res.*, *113*, C05008, doi:10.1029/2007JC004343.

1. Introduction

[2] The natural disaster caused by the earthquake and subsequent tsunami in the Indian Ocean on 26 December 2004 has led to a large number of recent publications on tectonics, earthquakes, tectonically generated water waves, and wave runup along the coastline. There is, moreover, an enhanced attention to potential generation of disastrous flood waves in the ocean, coastal waters, fjords/inlets, and lakes by submarine slides and landslides. Publications by, for example, *Liu* [2005], *Dalrymple et al.* [2006], *Glimsdal et al.* [2006], *Pelinovsky* [2006], *Liu et al.* [2008], and the references cited in the publications, describe recent progress of the analysis and prediction of tsunamis. This includes derivation of the basic equations and how they are simplified and solved numerically and implemented in larger computer codes for practical computations of the waves on ocean scale and in coastal water. The wave analysis codes are combined with seismic models which predict the motion of the seafloor that generates the waves. A recent book edited by *Yalciner et al.* [2003] is particularly devoted to slide-generated waves and runup on shore. Analysis and prediction of runup has recently been studied by *Didenkulova et al.* [2006] and *Kanoglu and Synolakis* [2006].

[3] Nonlinear shallow water theory (NLSW) has been implemented in the TUNAMI code for practical analysis of tsunamis [see *Intergovernmental Oceanographic Commission.*, 1997; *Zaitsev et al.*, 2005; *Pelinovsky*, 2006]. Other codes to predict tsunami motion on basin scale as well as in shallow seas, including the motion on shore, are described by *Dalrymple et al.* [2006]. They employ models like linear long-wave theory and NLSW and discuss the effect of frequency dispersion in terms of the Boussinesq equations. Predictions of runup using the FUNWAVE program and NLSW code agreed well with the ranges measured in field surveys after the 26 December 2004 tsunami in the Indian Ocean at a few locations along the coastline. They concluded, among other things, that the effect of dispersion should be included in the modeling in order to properly model the dispersive wave train following the leading tsunami. Formation of undular bores in shallow water was not discussed.

[4] Numerical results for the waves in the Bay of Bengal and wave runup at Banda Aceh and Yala/Sri Lanka were described by *Horrillo et al.* [2006] and *Ioualalen et al.* [2007]. Using the shallow water equations, a variant of the nonlinear Boussinesq equations, and the full Navier-Stokes equations, the latter implemented with a volume of fluid method, *Horillo et al.* [2006] were particularly looking for

[1]Mechanics Division, Department of Mathematics, University of Oslo, Oslo, Norway.
[2]Department of Nonlinear Geophysical Processes, Institute of Applied Physics, Nizhny Novgorod, Russia.
[3]Institute de Recherche sur les Phénomènes Hors Equilibre, Marseille, France.

0148-0227/08/2007JC004343$09.00

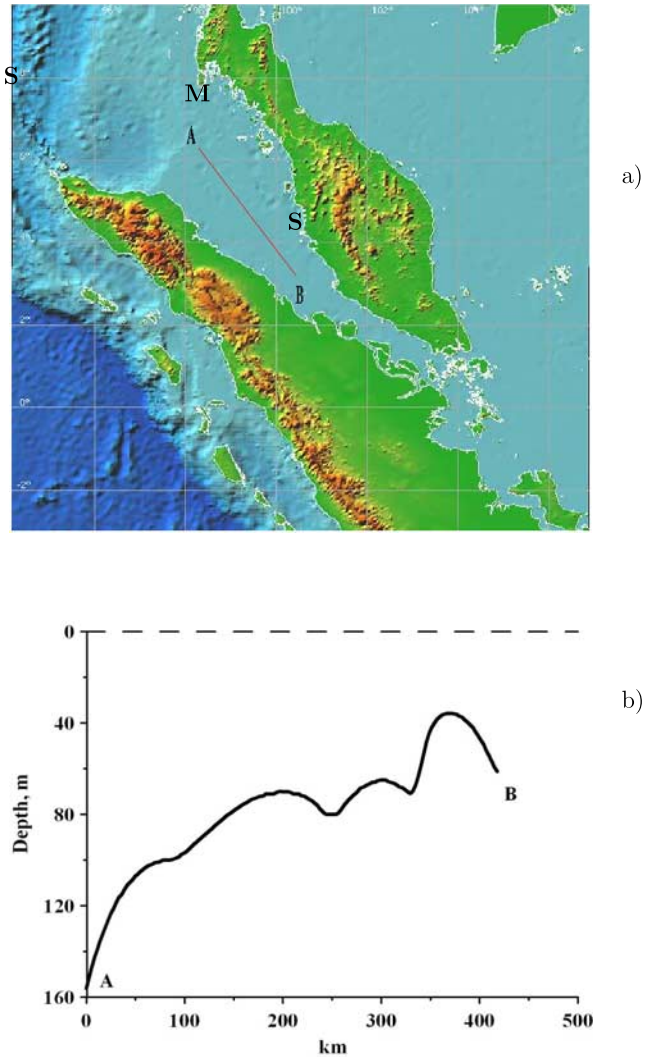

Figure 1. (a) The section A–B in the Strait of Malacca. Letter M marks the position of the yacht *Mercator*. The points S to S indicate the section studied by *Glimsdal et al.* [2006]. (b) Depth profile along the section.

the effect of dispersion on the generated waves. Predictions of the leading waves by the nonlinear Boussinesq and full Navier-Stokes equations agreed quite well but generally differed from the shallow water equations in that study. Formation of short undular bores was not discussed. Using the nonlinear long-wave equations and a variant of the modified momentum conservation equations, where nonlinearity, dispersion, the Coriolis force, and even baroclinicity and compressibility were accounted for, *Rivera* [2006] modeled the Indian Ocean tsunami. He primarily presented results regarding the initial drying and flooding of the coasts and compared the simulation to observations of sea elevation by satellite along its track. No attention was given to formation of undular bores in regions with shallow water.

[5] *Glimsdal et al.* [2006] performed simulations using several models, including the linear shallow water equations, a variant of the low-order Boussinesq equations, including weakly nonlinear and dispersive effects, and ray theory for linear hydrostatic waves. They investigated the waves due to four different source characteristics of the fault, concluding that the largest uncertainty in the wave computations of the Indian Ocean tsunami relates to the generation phase of the waves. While dispersion was not seen in the generation phase, this effect may modify the wave propagation slightly when the motion takes place over a long time and may become important in shallow water. Idealized simulations of one-dimensional wave propagation along a section in the shallow Strait of Malacca exhibited that an undular bore was generated in a region between 2 and 7 km from the shoreline, depending on the source characteristics of the fault. We shall compare our calculations to the results obtained by *Glimsdal et al.* [2006]; see section 3.8. Undular bores were also observed in calculations of the Nicaragua earthquake tsunami [see *Shuto*, 1985]. The generation process and potential formation of solitons in the shallow sea were not discussed.

[6] The present investigation focuses on undular bores and solitons that are generated by a long tsunami propagating into shallow water. Motivation comes from observations of short waves in the form of undular bores in the Strait of Malacca generated by the Indian Ocean tsunami; see video of possible breaking undular bore, Malaysia, 26 December 2004 (available at http://www.dagbladet.no/download/malaysia_wave.wmv) The video indicates a short-wave period of 15–20 s at the beach. Recent computations by *Pelinovsky et al.* [2005] using Korteweg-deVries (KdV) theory indicate that very short wave phenomena may take place during the motion in the shallow sea and that a fuller model than KdV is required to correctly model the formation of the short waves. The essential point here is to study the process where a long depression wave with a subsequent wave of elevation steepens in its back face during the propagation into shallow water and how a train of short waves is generated in the back face of the leading depression.

[7] We model the wave motion along a 420 km long section, given as A–B which is midway between Sumatra Island and the Malaysian Peninsula; see Figure 1a. The depth profile of the sea is indicated in Figure 1b, ranging from 156 m at position A (the starting point) and reducing to 70 m at the first of three bottom ridges after 200 km. The two other ridges have depths of 65 and 36 m and are located after 300 and 375 km, respectively.

[8] The wave motion at the entrance of the strait results from a realistic simulation of the Indian Ocean tsunami and is used as initial condition in the computations of the motion in the strait. The input wave is characterized by a leading depression and subsequent elevation and has a height that corresponds to observations at a yacht located outside Phuket, somewhat north of the starting point of the simulation; see Figure 2c and the video of tsunami observations by the echo sounder on yacht *Mercator*, Phuket (available at http://www.knmi.nl/VinkCMS/news_detail.jsp?id = 19222).

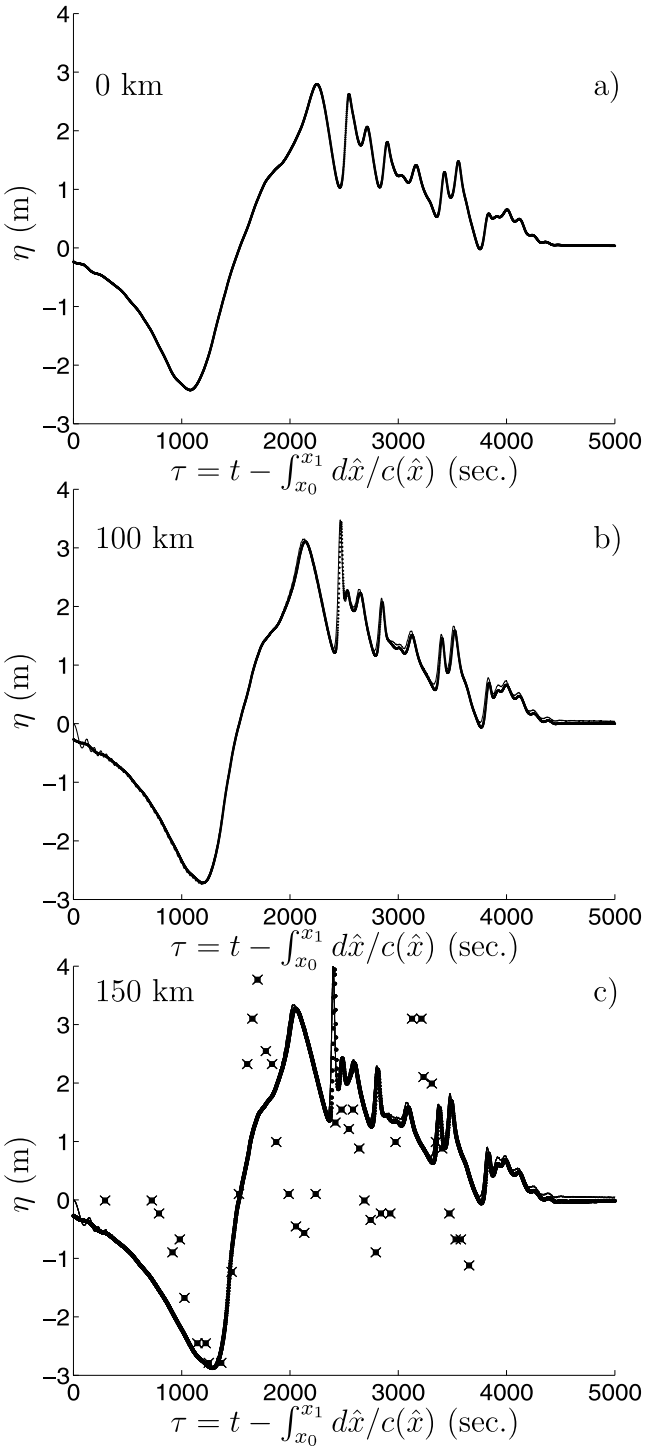

Figure 2. Time history of η: (a) 0 (initial condition), (b) 100, and (c) 150 km. Full solution (dots) is t = tkdv + 3007 s (100 km) abd t = tkdv + 4715.3 s (150 km). KdV is shown by the line; The × indicates the observed elevations made at the yacht *Mercator* (reference) near Phuket.

[9] Two models are used to predict the wave motion: a weakly nonlinear dispersive Korteweg-de Vries model and a fully nonlinear and fully dispersive model (the full Euler equations) derived recently by *Fructus and Grue* [2007]. Descriptions of the models are given in section 2. Results of the simulations are described in section 3. Summary and conclusions are given in section 4.

2. Models

[10] The two models in use are a weakly nonlinear dispersive KdV model, valid for one-directional wave propagation, and a fully nonlinear and fully dispersive model in three dimensions, run here for two-dimensional calculations along the section, allowing for two-directional wave motion.

2.1. Korteweg-de Vries Model

[11] During the past decades, nonlinear dispersive models were developed to study tsunami propagation. They are based on various extensions of the Boussinesq equations. *Hammack* [1973], *Murty* [1977], and *Mirchina and Pelinovsky* [1982, 1984] gave rough estimates for the applicability of weakly nonlinear dispersive theory based on the Korteweg-de Vries equation for constant water depth, and *Mirchina and Pelinovsky* [1982] used the database for tsunamis in the period 1896–1968 (27 events) to show that some of the cases fall into the category of nonlinear dispersive tsunamis. *Gonzales and Kulikov* [1993] and *Kulikov and Gonzales* [1995] reported tsunami dispersion observed in the deep ocean. *Satake* [1995] investigated the nonlinear effects in the 1992 Nicaragua tsunami. A variant of the weakly nonlinear dispersive models is a generalized KdV equation, and it is useful for one-directional weakly nonlinear dispersive wave motion [*Ostrovsky and Pelinovsky*, 1970; *Johnson*, 1972; *Voit*, 1987; *Pelinovsky*, 1996; *Johnson*, 1997; *Caputo and Stepanyants*, 2003]:

$$\frac{\partial \xi}{\partial x} - \frac{3\xi Q(x)}{2h(x)c(x)}\frac{\partial \xi}{\partial \tau} - \frac{h(x)^2}{6c(x)^3}\frac{\partial^3 \xi}{\partial \tau^3} = 0, \tag{1}$$

where x denotes the horizontal coordinate, t is time, and

$$\eta(x,t) = \xi(\tau,x)Q(x), \quad \tau = t - \int \tfrac{dx}{c(x)}, \qquad c(x) = \sqrt{gh(x)}, \qquad Q(x) = \left[\tfrac{h}{h_0}\right]^{-\frac{1}{4}}. \tag{2}$$

Further, η denotes surface elevation, $h(x)$ is water depth, h_0 is water depth at the starting point of the wave (taken to be point A in Figure 1), and g is acceleration of gravity. Numerical solution of the KdV equation with variable coefficients is calculated using a finite difference scheme described by *Berezin* [1987]. Periodic boundary conditions are applied in the temporal domain, 0 s < τ < 7200 s, and the number of points is 10.000 (in the τ range, i.e., $\Delta\tau$ = 0.72 s). The time step was chosen from the Courant criterion.

2.2. Fully Nonlinear Dispersive Method

[12] Fully nonlinear dispersive methods (FNDM) for rapid computations of nonlinear wave motion in three dimensions have been developed in recent years by means of pseudospectral methods [e.g., *Bateman et al.*, 2001; *Clamond and Grue*, 2001; *Grue*, 2002; *Fructus et al.*, 2005] and highly nonlinear Boussinesq equations [e.g., *Madsen et al.*, 2002]. The highly nonlinear Boussinesq

equations were developed to also study wave motion interacting with a variable (and/or moving) sea bottom [e.g., *Lynett and Liu*, 2002]. The pseudospectral method of *Clamond and Grue* [2001], *Grue* [2002], and *Fructus et al.* [2005] was recently extended by *Fructus and Grue* [2007] to compute fully nonlinear dispersive wave motion in three dimensions over moving or nonmoving variable bathymetry. The resulting expressions were obtained in explicit form with evaluations using fast Fourier transform (FFT). The method is very rapid.

[13] We shall perform fully nonlinear dispersive computations of the wave motion using the method of *Fructus and Grue* [2007]. A short account of the method is given here. Fully nonlinear motion of the free surface over variable bottom topography in three dimensions is modeled, assuming a fluid that is homogeneous and incompressible and that the motion is irrotational. Let $\mathbf{x} = (x_1, x_2)$ denote the horizontal coordinate, y is the vertical coordinate, and t is time. Let $y = 0$ represent the still water level and $y = \eta(\mathbf{x}, t)$ represent the surface elevation. The bottom topography is represented by $y = -h_0 + \delta(\mathbf{x}, t)$, where in the special case of a flat bottom located at $y = -h_0$ the variable $\delta(\mathbf{x}, t)$ is identically zero. Let ϕ denote the velocity potential, $\nabla = (\partial/\partial x_1, \partial/\partial x_2)$ is the horizontal gradient, and grad ϕ is the three-dimensional velocity field. Subscript "s" is used to denote quantities at the free surface, e.g., $\phi_s(\mathbf{x}, t) = \phi[\mathbf{x}, y = \eta(\mathbf{x}, t), t]$, and subscript "b" is used to denote quantities at the sea bottom, e.g., $\phi_b(\mathbf{x}, t) = \phi[\mathbf{x}, y = -h_0 + \delta(\mathbf{x}, t), t]$.

[14] The kinematic and dynamic boundary conditions at the free surface may be written [*Grue*, 2002, equations (3) and (4)]:

$$\partial\eta/\partial t - V_s = 0, \tag{3}$$

where

$$V_s = \partial\phi/\partial n\sqrt{1+|\nabla\eta|^2},$$
$$\partial\phi_s/\partial t + g\eta + \frac{|\nabla\phi_s|^2 - V_s{}^2 - 2V_s\nabla\eta\cdot\nabla\phi_s + |\nabla\eta\times\nabla\phi_s|^2}{2\left(1+|\nabla\eta|^2\right)} = 0, \tag{4}$$

where the unit normal vector, n, is pointing out of the fluid.

[15] The (scaled) normal velocity at the free surface, V_s, and the velocity potential at the seafloor, ϕ_b, are obtained by the solution of a coupled set of integral equations. These are derived from the solution of the Laplace equation. For an evaluation point that is on the free surface, we obtain

$$\int_{\mathcal{S}+\mathcal{B}}\left(\frac{1}{\tilde{r}}+\frac{1}{\tilde{r}_{\mathrm{B}}}\right)\frac{\partial\phi'}{\partial n'}\,\mathrm{d}S' = 2\pi\phi + \int_{\mathcal{S}+\mathcal{B}}\phi'\,\frac{\partial}{\partial n'}\left(\frac{1}{\tilde{r}}+\frac{1}{\tilde{r}_{\mathrm{B}}}\right)\mathrm{d}S', \tag{5}$$

where $\tilde{r}^2 = R^2 + (y' - y)^2$, $\tilde{r}_{\mathrm{B}}^2 = R^2 + (y' + y + 2h_0)^2$. The horizontal distance between the primed and unprimed positions is denoted by $R = |\mathbf{x}' - \mathbf{x}|$. Further, $\mathcal{S}$ denotes the instantaneous free surface, and $\mathcal{B}$ denotes the sea bottom. Equation (5) and a similar equation that is valid when the field point is located at the sea bottom are used to derive explicit formulas for the evaluation of V_s [see *Fructus and Grue*, 2007], giving for rigid sea bottom (the case of a moving bottom topography is included in the formulation by Fructus and Grue):

$$\mathcal{F}\left(V_s^{(1)}\right) = k\tanh kh_0\mathcal{F}(\phi_s), \quad \mathcal{F}\left(\phi_b{}^{(1)}\right) = \mathcal{F}(\phi_s)/\cosh kh_0, \tag{6}$$

$$\mathcal{F}\left(V_s^{(2)}\right) = \mathcal{F}\left(V_s^{(1)}\right) - \left[k\tanh kh_0\mathcal{F}\left(\eta V_s^{(1)}\right) + \mathrm{i}\mathbf{k}\cdot\mathcal{F}\{\eta\nabla\phi_s\} - \mathrm{i}\mathbf{k}\cdot\mathcal{F}\left\{\delta\nabla\phi_b{}^{(1)}\right\}/\cosh kh_0\right], \tag{7}$$

$$\mathcal{F}\left(\phi_b^{(2)}\right) = \mathcal{F}\left(\phi_b^{(1)}\right) - \mathcal{F}\left(\eta V_s^{(1)}\right)/\cosh kh_0 - \mathrm{i}\tanh kh_0\mathbf{k}\cdot\mathcal{F}\left\{\delta\nabla\phi_b{}^{(1)}\right\}/h_0, \tag{8}$$

$$\mathcal{F}\left(V_s^{(3)}\right) = \mathcal{F}\left(V_s^{(2)}\right) - \left\{k\tanh kh_0\mathcal{F}\left[\eta\left(V_s^{(2)} - V_s{}^{(1)}\right)\right] - \frac{k^2}{2}\mathcal{F}\left(\eta^2 V_s{}^{(1)}\right)\right\} + \frac{k}{1+e_h}\cdot\left\{\mathcal{F}\left(\eta\mathcal{F}^{-1}[-\mathrm{i}\mathbf{k}\cdot\mathcal{F}\{\eta\nabla\phi_s\}]\right) + \mathrm{i}\frac{e_h}{2}\mathbf{k}\cdot\mathcal{F}\left\{\eta^2\nabla\phi_s\right\} - \mathcal{F}\left\{\eta^2\mathcal{F}^{-1}\left[\frac{k^2}{2}\phi_s\right]\right\}\right\} + \frac{2\mathrm{i}\sqrt{e_h}}{1+e_h}\mathbf{k}\cdot\mathcal{F}\left\{\delta\nabla\left(\phi_b^{(2)} - \phi_b{}^{(1)}\right)\right\}, \tag{9}$$

where the formulas are obtained in Fourier space, $\mathcal{F}$ denotes the Fourier transform, $\mathcal{F}^{-1}$ denotes the inverse transform, $\mathbf{k}$ denotes the wave number in Fourier space, $k = |\mathbf{k}|$, and $e_h = \exp(-2kh_0)$.

[16] $V_s^{(3)}$ obtained by equation (9) provides an explicit inversion of the Laplace equation and is a highly accurate approximation to the fully nonlinear V_s [see *Fructus and Grue*, 2007]. Its evaluation by FFT is very rapid. The linear part of equations (3) and (4) with $V_s^{(3)}$ obtained by equation (9) is integrated analytically in time (in Fourier space), and the nonlinear part is integrated by a Runge-Kutta, fifth-forth order, combined (RK-5-4) procedure. An antialiasing strategy, where the spectra in Fourier space are doubled and the upper half of the Fourier coefficients are padded to zero, has been implemented. This removes the effect of aliasing in products up to cubic order. There is no smoothing or regridding in the computations. For further documentation of the time integration, see *Clamond et al.* [2007].

[17] In the present simulations, the FNDM is run with two discretizations, one coarse with $\Delta x = 40$ m and one fine with $\Delta x = 20$ m, giving the same result. (Very coarse discretization gives poor representation of the short waves.) The numerical tank is 715.7753 km plus 715.7753 km long, since it is continued symmetrically at the end for periodicity. Point A (defining $x = 0$) is located 176.08 km from the point where the numerical tank begins (at $x = -176.08$ km). After point B and until 715.7753 km the bottom is set to a constant level and then continued symmetrically. For further

documentation of the practical spacial integration, see *Fructus et al.* [2005].

3. Simulations

3.1. Input Wave

[18] The input wave to the present computations was obtained from calculations of the 26 December 2004 tsunami using the TUNAMI code (see section 1). In this code the linear long-wave equations are used to model the motion in the open ocean, taking into account the curvature and rotation of the Earth and the wave dissipation in the turbulent boundary layer at the ocean bottom. In the coastal zone, having relatively small scales (up to 1000 km), the nonlinear motion is modeled in the tangent plane with the effect of rotation discarded. A radiation condition is applied at the open boundaries of the computational domain. Total reflection is assumed along the coastline. The initial water displacement in the source is determined using seismological models.

[19] Numerical simulations of the Indian Ocean tsunami using the TUNAMI code were presented by *Zaitsev et al.* [2005]. They used a model source that also was applied by many other researchers immediately after the event (in January 2005). Their Figure 1b (not shown here) shows the numerical sea level in the Indian Ocean after 2 h and, important for our analysis, a leading wave of depression and subsequent wave of elevation moving into the Strait of Malacca at the entrance. The wave crest is slightly crescent-shaped: the part extending between Sumatra Island and about halfway into the strait has orientation orthogonal to the midsection of the strait, while the remaining crest is bending against the Malaysian Peninsula. Independent simulations confirm a main wave propagation direction along the midsection of the strait, with crest bending toward the coastlines at both sides [e.g., *Glimsdal et al.*, 2006].

[20] We derive our input wave from the time history of the wave, produced by the TUNAMI code, observed at point A. This point is indicated in Figure 1a. We study the resulting wave motion along section A–B midway in the strait, also indicated in Figure 1a. We assume that the input wave has the form $\eta(t-x/\sqrt{gh_0})$, where at point A, x is set to zero. Here x denotes the coordinate along midsection A–B, and h_0 is the water depth at point A. The input time history of $\eta(t)$ with $x = 0$, also discussed by *Pelinovsky et al.* [2005], is shown in Figure 2a. This time history is used directly as input to the KdV model. The fully nonlinear dispersive calculations require both surface elevation and wave potential as input at $t = 0$. While the surface elevation is obtained by $\eta(t-x/\sqrt{gh_0})$ at $t = 0$, we also extract its time derivative by $\eta_t(t-x/\sqrt{gh_0})$ and use this function as input to the set of integral equations to find the wave potential at $t = 0$.

[21] The initial wave height is 5.2 m (Figure 2a) which amounts to 3% of the water depth of 156 m at position A. The period of the incoming wave is about 4500 s, and length is about 176 km (the total). The trough-to-crest period is 1000 s, corresponding to 17 min, and length is 39 km. The maximal slope of the initial wave is up to $\eta_x = 0.02 \times 10^{-3}$ in the back face of the leading depression wave. The very small slope of the seafloor along section A–B of about 0.3×10^{-3} means that the wave reflection should be small, which is one of the requirements for the use of the KdV model. While the KdV model is limited to the weakly nonlinear dispersive regime, the full model used here is valid for any nonoverturning and dispersive wave motion and any nonoverhanging variation of the seafloor in three dimensions.

[22] For comparison, we also perform a simulation with half amplitude of the input wave defined in Figure 2a. The initial wave height is then 2.6 m. Results are presented in section 3.6.

3.2. Comments on the Input Wave

[23] A proper modeling should ideally include a two-dimensional bathymetry and effects of diffraction and refraction, both important for tsunami behavior near the coast. However, a three-dimensional simulation of tsunamis in the shallow strait, taking into account bottom dissipation, sidewalls, beaches, and wave breaking (which is expected from our simulations), is problematic, and it is not the main goal of our paper. Instead, we aim to document the importance of strong nonlinear and dispersive effects to the modeling of real tsunami motion in restricted water through study with an initial quasi-real waveshape. The most important features of the input wave include a realistic height, leading depression, and front part of subsequent crest. The motion behind the crest where short-wave phenomena are observed, being a result of complicated diffraction patterns, is irrelevant to the formation of undular bores and solitons since the latter are generated in the back face of the leading depression (see section 3.4).

[24] Reflection from the coast may not be important to the front part of the wave motion since the distance to coast in transversal direction is large. Moreover, reflection due to bottom topography is very small since the depth along the section varies smoothly, as also documented by *Pelinovsky et al.* [2005], where simulations using the TUNAMI model and KdV compared favorably for the low-frequency part of the motion. Refraction effects were estimated by Pelinovsky et al., evaluating the distance between neighboring rays (ray theory) and finding even better agreement in the wave amplitude. Such an approach is effective in KdV models but is not applicable to fully nonlinear models. Taking into account that we wish to investigate strongly nonlinear effects, we may in the first approximation neglect three-dimensional effects.

[25] The wave evolution studied here produces a lot of very short solitons of large amplitude. Real three-dimensional effects will influence amplitudes and number of solitons, of course. Questions that remain to be answered include the following: What is the end result of such an evolution? How will the group of solitons dissipate because of breaking? Which kind of secondary effects will be manifested: formation of uniform flow again, with no solitons? Here we have chosen to perform a model study, where the main purpose is to illuminate the formation process of undular bores and their subsequent development into solitons, leaving the other issues for future study.

3.3. Steepening of the Back Face of the Depression Wave

[26] The plots in Figure 2 illustrate how the wave evolves during the first 150 km of the shallow strait. Both models

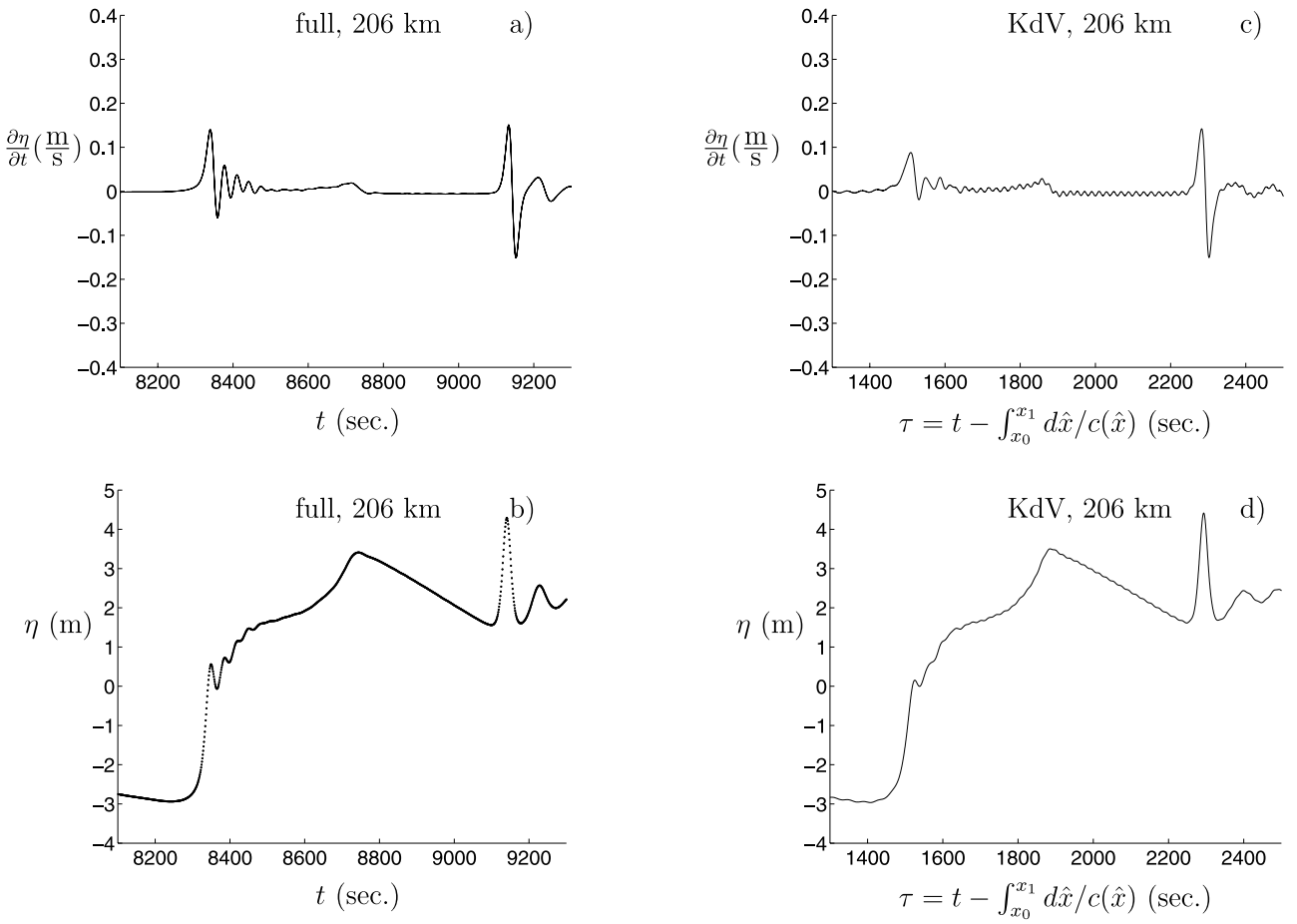

Figure 3. Time series of elevation η (in meters) and its time derivative $\partial\eta/\partial t$ (in m/s) at 206 km; full solution and KdV.

predict the same wave behavior. While the KdV equation is integrated here in the frame of reference moving with the shallow water speed, as a function of the horizontal coordinate, the grid is fixed in the FNDM. Both models predict a significant steepening of the back face of the leading depression wave which also increases somewhat in height while moving into the region with decaying water depth. Estimates of maximum of η_t in the back face of the leading depression wave show that this is up to 0.024 m/s at 150 km for both models, indicating also the maximum vertical velocity of the water surface at the registration point. The corresponding wave slope becomes $\eta_x \simeq \eta_t / \sqrt{gh} \simeq 0.87 \times 10^{-3}$ (at 150 km).

[27] The second crest of the input wave becomes relatively steep during the propagation. This crest remains almost unchanged during the subsequent motion, however, and is not important to the formation of the short waves; see the results that are presented in Figures 3–6.

[28] In Figure 2c we have included a recording of the tsunami made at the yacht *Mercator* in 12 m depth outside Phuket. The location of the yacht was north of starting point A of the present simulations and is marked by the letter M in Figure 1a. The input wave height predicted by the TUNAMI simulation corresponds fairly well to the observation at *Mercator*. Further, the maximum value of η_t in the simulation after 150 km of wave propagation in the shallow sea is similar to the wave that was observed at *Mercator*. (Note that the wave slope at *Mercator* is 2.5 times higher than at the 150 km position since the wave is relatively much shorter in water of 12 m depth compared to 80 m depth.)

3.4. Formation of Undular Bore

[29] Undular bores form when the ratio of the change in water level to the undisturbed water depth is less than 0.28 according to the experiments by *Favre* [1935]. There are still undulations if this ratio is in the range between 0.28 and 0.75, but the first undulation, at least, is breaking [*Binnie and Orkney*, 1955]. For greater differences in depth there are no undulations. *Keulegan and Patterson* [1940] showed that the undulations measured by Favre had properties close to those of cnoidal waves, with the solitary waveform in the limit as the wavelength increased. *Peregrine* [1966] performed computations of the growth of an undular bore from a long wave of elevation of initially gentle slope, integrating the KdV equation. Below we compare our results with those of Peregrine.

[30] In the present computations the initial wave height of 5.2 m divided by water depth is up to 0.074 at the first ridge, where the train of short waves appears for the first time, meaning that the flow falls into the category of a nonbreaking undular bore. Steepening of the back face of the

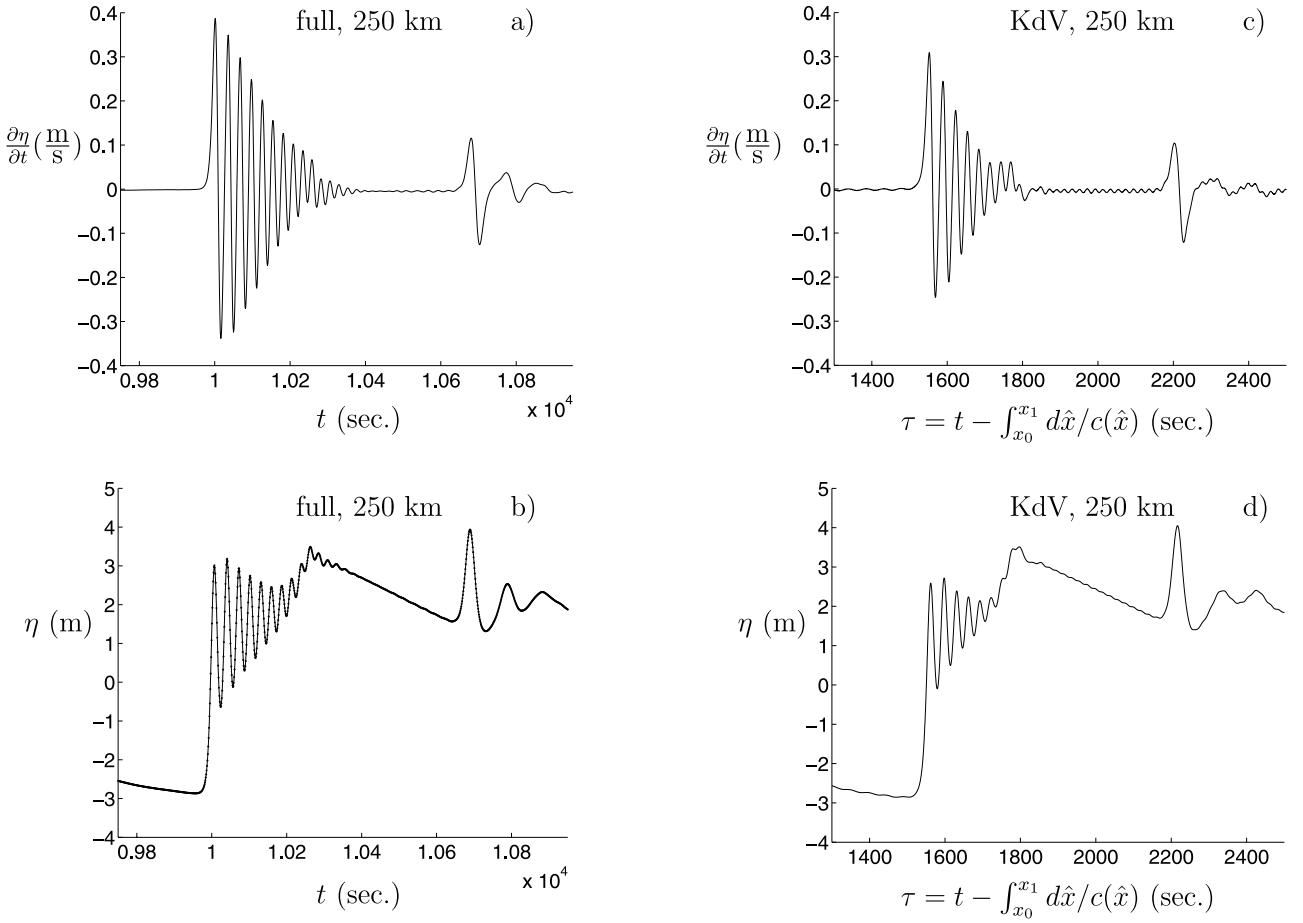

Figure 4. Same as Figure 3 but at 250 km.

leading depression wave develops during the wave motion. The maximum of η_t amounts to 0.1 m/s at 200 km in the FNDM. The corresponding wave slope is $\eta_x \simeq \eta_t/\sqrt{gh} \simeq 3.8 \times 10^{-3}$. At 206 km η_t amounts to 0.14 m/s ($\eta_x = 5.3 \times 10^{-3}$) in the FNDM and 0.088 m/s ($\eta_x = 3.3 \times 10^{-3}$) in KdV (corresponding to 63% of the full model). A group of short waves appears for the first time in the rear of the leading depression wave (see Figure 3). The short waves appear for η around zero. Initially, the waves have very small amplitude and exhibit a linear behavior. They become more enhanced and visible when plotting the time history of the time derivative of the elevation (see the plots in Figures 3a and 3c). The short waves appear in a similar way in both models, but the full prediction gives about 50% larger height for the short waves at 206 km compared to the KdV model.

[31] The short waves are characterized by a leading wave with period of 35 s. The wave number is estimated by the linear dispersion relation when the short waves are small, i.e.,

$$\omega^2 = gk \tanh kh. \tag{10}$$

This gives $\omega^2 h/g \simeq 0.23$ and $kh \simeq 0.5$ for $\omega = 2\pi/35\ \mathrm{s}^{-1}$, corresponding to a wavelength of 880 m; it is about 4π times the local depth of $h = 70$ m. At 206 km the wave height of the leading short wave is about 60 cm and grows quickly. The energy supply to the wave group comes from the continuous steepening of the back face of the long depression wave during its propagation in the shallow water. The generation of the short-wave train helps brake the steepening of the main wave.

[32] At 206 km the total period of the short-wave group is about 130 s, while at 250 km (Figure 4) this period has grown to about 350 s. (The local wave period at 250 km is 33 s.) The computations show that the front of the short-wave group spends a travel time of 1657.5 s on the 44 km distance between positions at 206 km and 250 km. This gives an average speed of 26.5 m/s and corresponds well to the shallow water speed $c = \sqrt{gh}$ which equals 26.2 m/s with $h = 70$ m and 28 m/s with $h = 80$ m, the latter depth at 250 km.

[33] The tail of the wave train spends the longer time of 1877.5 s on the 44 km long distance, corresponding to an average speed of 23.4 m/s. The tail of the wave train propagates with the group velocity which may be estimated from the linear dispersion relation (10) giving

$$c_g = \frac{\partial \omega}{\partial k} = \frac{g \tanh kh}{2\omega}\left(1 + \frac{2kh}{\sinh 2kh}\right) \simeq 23.4 \text{ m/s for } kh = 0.5,$$
$$\omega = 2\pi/35\mathrm{s}^{-1},$$

indicating good correspondence with the computations.

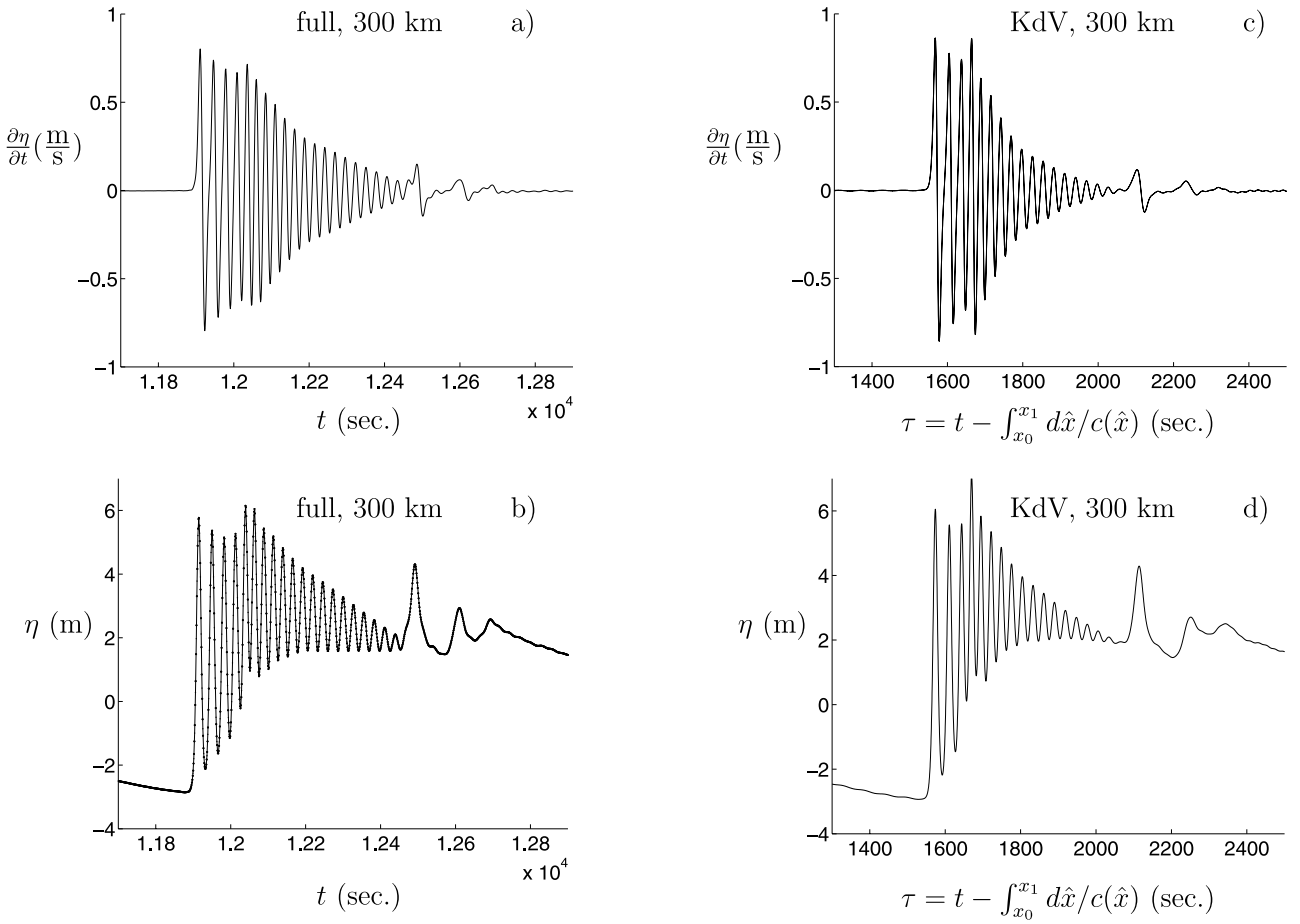

Figure 5. Same as Figure 3 but at 300 km.

3.4.1. Growth Rate of Undular Bore

[34] The growth rate of the amplitude of the undular bore, in its initial phase, may be estimated by using the KdV equation. Assuming for the moment that the main wave satisfies the KdV equation, that the train of short waves satisfies the linearized KdV equation, and that the train of short waves may locally be described by $a(x, t)\cos(kx - \omega t + \delta_0)$, where a denotes amplitude, δ_0 is phase, k is wave number, and ω is frequency, an equation for the growth of the amplitude is derived, to leading approximation,

$$\frac{\partial a}{\partial t} - \frac{3}{2}\frac{\eta_t}{h}a = 0, \tag{11}$$

giving

$$a(t) = a(t_1)e^{\frac{3\eta_t}{2h}(t-t_1)}, \tag{12}$$

where we have used $\eta_t \simeq -\eta_x \sqrt{gh}$ and assumed that η_t locally is constant (in the initial phase). The FNDM shows that the crest-to-trough height of the leading undulation grows from 0.3 m at 200 km to 0.7 m at 206 km during a time period of 250 s, where η_t is 0.1 m/s at 200 km and 0.14 m/s at 206 km. Fitting $\eta_t = 0.14$ m/s, t-$t_1 = 250$ s, and $h = 70$ m into (11) predicts a growth of the amplitude of 2.12 and is relatively close to growth of 0.7/0.3 = 2.33 observed in the FNDM.

3.4.2. Comparison to *Peregrine*'s [1966] Calculations of Undular Bores

[35] The maximum value of $\partial\eta/\partial t/\sqrt{gh}$ in the present computations is 0.0038 at 200 km (results not shown), 0.0053 at 206 km (Figure 3a), 0.0134 at 250 km (Figure 4a), 0.0314 at 300 km (Figure 5a), 0.0467 for the first wave at 350 km, and 0.0667 for the second wave at 350 km (Figure 6a). The KdV computation in Figure 6c exhibits a maximum of $\partial\eta/\partial\, t/\sqrt{gh}$ of 0.141 at 350 km. These values may be compared to the computations by *Peregrine* [1966] of an undular bore, where, from his results, we estimate that $\partial\eta/\partial\, t \simeq 0.02\sqrt{gh}$ in one example, $\partial\eta/\partial t \simeq 0.033\sqrt{gh}$ in another example, and $\partial\eta/\partial t \simeq 0.06\sqrt{gh}$ in his strongest example, which means that our and his calculations are in the same range, except, possibly, our KdV computation at 350 km shown in Figure 6c.

[36] Peregrine's computations exhibit a wavelength of the leading undulation in the range 7–8 times the water depth, corresponding to $kh \simeq 0.8$–0.9, and a wavelength behind the leading undulation of about $6h$, corresponding to $kh \simeq 1$, meaning that his waves were shorter than in the present computations. We note that the relatively short waves that he computed were outside the range of validity of the KdV equation that he used.

[37] Although maximum values of $\partial\eta/\partial\, t/\sqrt{gh}$ are similar in our and Peregrine's computations, the relative change in water depth is much smaller here (0.074) than in his work

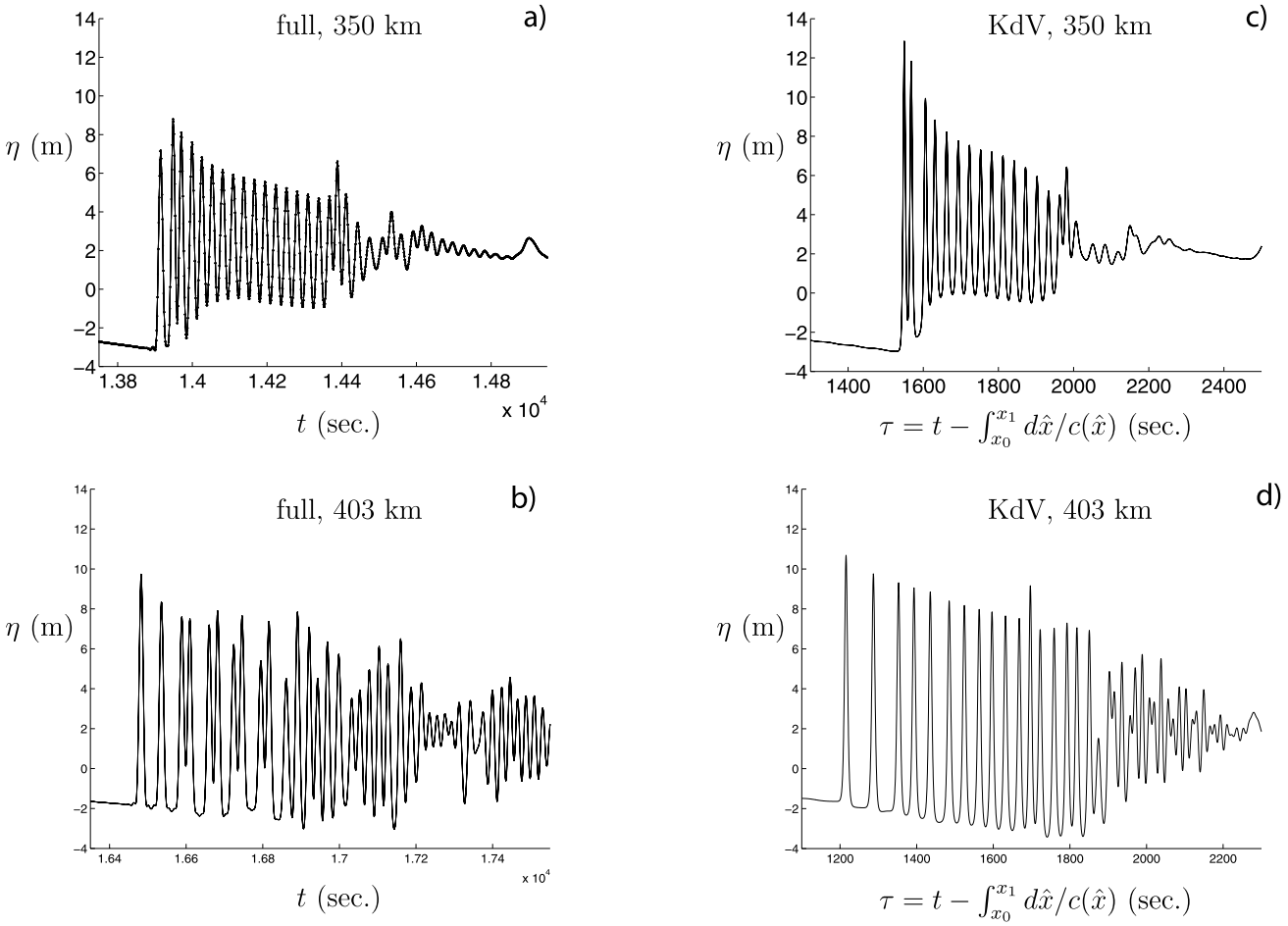

Figure 6. Time series of elevation η (in meters) versus time at positions 350 and 403 km for full solution and KdV.

(up to 0.2). The undulations have consequently relatively higher amplitude here. He showed no results on the formation of solitons.

3.4.3. Nonlinear Interfacial Undular Bores

[38] Similar formation of interfacial undular bores, with subsequent formation of interfacial solitary waves, occurs in the layered ocean and is caused by tidal flow over subsea ridges or shelves. Fully nonlinear interfacial calculations exhibited linear behavior of the wave train in the generation phase, with wave number times the thinner layer depth about unity, and subsequent formation of interfacial solitary waves of large amplitude [see *Grue*, 2005, 2006].

3.5. Formation of Solitary Waves

[39] At 300 km the group of short waves has increased in both length and amplitude (Figure 5). At this position, located between the second and third peak in the bottom profile, there is relatively good agreement between the FNDM and KdV. Both methods predict the same behavior of the leading depression and elevation parts in the tail of the wavefield. The leading wave of the wave group predicted by the full model has developed into a KdV soliton and is confirmed by fitting the function $\bar{a}\ \mathrm{sech}^2[\sqrt{3\bar{a}/4\bar{h}}(x-ct)/\bar{h}]$ and $c=\sqrt{g(\bar{h}+\bar{a})}$, where $\bar{a}$ denotes the wave height relative to the local mean water level and $\bar{h}$ is the local mean water depth (see Figure 7a). The soliton behavior in the lead of the short-wave train is slightly different in the two models, however.

[40] The water depth is reduced to 44 m at 350 km, reduces further to 36 m at 375 km, and increases to 47 m at 403 km. The small depth influences the train of short waves significantly as visualized in Figure 6 at 350 km and 403 km. There is an enhanced effect of the local nonlinearity, and it may be illustrated by the nonlinear parameter derived from the full solution, which becomes $\bar{a}/\bar{h}$ = 0.13 (300 km), 0.27 (350 km), 0.41 (375 km), and 0.32 (403 km), where $\bar{a}$ is the wave height relative to the local mean water level and $\bar{h}$ is the local mean water depth. At 350 km there are notable differences between the FNDM and KdV. The leading solitary wave in the FNDM is wider than the KdV soliton (Figure 7b). The KdV solver predicts leading wave heights that exceed the full solution by about 50%. The wave motion is similar in the two models at 403 km when the third bottom peak is passed, however. The leading waves of the group are pulse-like and are predicted somewhat differently by the two models. All of the individual elevation waves will eventually develop into solitary waves. Strong interactions between the individual waves following the leading ones are observed. At 403 km the predicted period between the two leading solitary waves is approximately

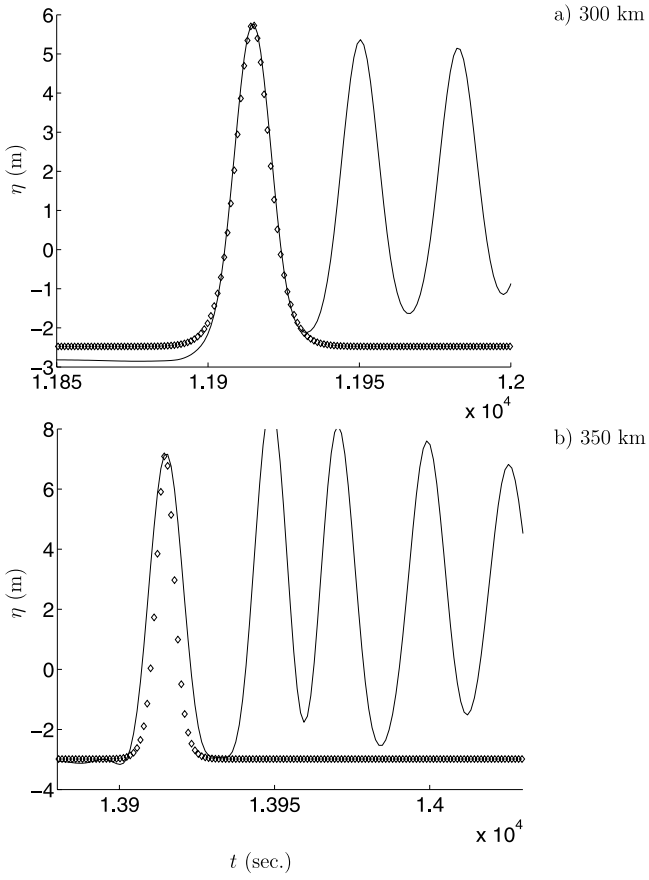

Figure 7. Fitted KdV soliton (diamonds) versus full solution (solid line) at (a) 300 and (b) 350 km.

54 s in the FNDM and 72 s in KdV, and amplitudes are about 10% higher with KdV than with the full method. An estimate of the peak-to-peak wavelength is obtained by multiplying the period with the nonlinear wave speed, giving a separation of 29 and 39 times the water depth, respectively. This distance is increasing with time according to the wave speed of the individual solitons. The short solitary waves of elevation have a greater speed than the long leading wave of depression and thus advance along the depression wave. The global wave height is twice that of the input wave.

3.5.1. Evaluation of the Ursell Number

[41] We evaluate the Ursell number for the leading waves, defined by $a/k^2h^3 = 0$ (206 km), 1 (300 km), 3 (350 km), 1.1 (375 km), and 0.48 (403 km).

3.5.2. Comments on Soliton Fission

[42] It has been found both numerically and experimentally that a soliton traveling from one constant depth to another constant but smaller depth disintegrates into several solitons of varying sizes with an oscillatory wave train in the tail. Analysis of this fission was based on the application of the KdV equation [see *Mei*, 1989, p. 560]. (We note that the fully nonlinear scenario may deviate from what can be deduced from KdV theory, as illustrated in the present computations.) The results in Figure 6 indeed illustrate that the waves of elevation are undergoing significant modification and interaction during their motion along the leading wave of depression. One may use the term fission in a more generalized sense where the steep front of a wave of elevation (in the present study, the steep back face of the leading depression) disintegrates into a number of short waves of initial linear behavior, growing in amplitude and developing eventually into a train of solitary waves.

3.6. Simulations With an Input Wave of Half Amplitude

[43] We have also performed a numerical computation with the height of the initial wave, shown in Figure 2a, multiplied by one half, with results shown in Figure 8. In this case there is no short-wave generation until the wave-front arrives at 350 km. The maximal value of η_t is 0.075 m/s in the back face of the leading depression wave at 350 km. This corresponds to a wave slope of $\eta_x = \eta_t/\sqrt{gh} \simeq 3.6 \times 10^{-3}$ (h = 44 m) and is (about) the same slope as in the previous simulation where the short waves emerged at 200 km (see section 3.4). The period of the short waves at 350 km is about 45 s (see Figures 8a and 8b), corresponding to $\omega^2 h/g = 0.087$, $kh = 0.3$ using the linear dispersion relation, and a wavelength of about 920 m.

[44] A train of short waves develops when the steep front passes by the subsea ridge at 375 km (h = 36 m). At 375 and 403 km the train of short waves has a leading peak-to-peak height of about 3 m. The global wave height has reached about 4 m and is 50% higher than the initial wave height of 2.6 m. The leading short wave has a period of 30 s, while the wave period in the tail of the train is about 21.5 s. This gives $\omega^2 h/g = 0.313$ (with h = 36 m), $kh = 0.59$, and a corresponding wavelength of 382 m. The propagation time of the wave front of 1330 s from 350 to 375 km gives an average speed of 18.8 m/s and is close to the shallow water speed of 19 m/s at 375 km. The propagation time of the end of the wave train between the positions is estimated to be 1550 s, giving an average speed of 16.1 m/s. The group velocity corresponds to the wave train with a period of 21.5 s, and $kh = 0.59$ is $c_g = \frac{1}{2}(g/\omega)\tanh kh(1 + 2\,kh/\sinh 2kh) \simeq 16$ m/s and corresponds well with the computation.

3.7. Energy Transfer From Long to Short Modes

[45] The energy transfer from long to short modes may be visualized by plotting $\mathcal{F}_0(\eta_t) = \int_{-\infty}^{\infty} e^{-i\omega t}\eta_t(t)dt$ as a function of ω. Figure 9a plots $|\mathcal{F}_0(\eta_t)|$ versus ω, using the original input wave with a height of 5.2 m, at 0 (initial), 250, and 403 km. The upshift of energy is evident. The peak frequency at 250 km is $\omega_p = 10^{-0.631}\mathrm{s}^{-1}$ corresponding to a wave period of 29.6 s. The peak frequency at 403 km is $\omega_p = 10^{-0.514}\mathrm{s}^{-1}$ corresponding to a wave period of 20.5 s. Both peak periods fit rather well with those observed in Figures 4 and 6, respectively. Results with the initial amplitude reduced to one half show a similar energy transfer (see Figure 9b). The peak frequency at 403 km becomes $\omega_p = 10^{-0.539}\mathrm{s}^{-1}$ with the 2.6 m wave, corresponding to a wave period of 20.7 s, and is almost the same as with the 5.2 m wave. Thus, the energy transfer in the end of the propagation is similar for the two input waves, indicating also that the bottom topography plays a fundamental role in the energy transfer. The energy transfer develops at a later stage for the smaller wave, however.

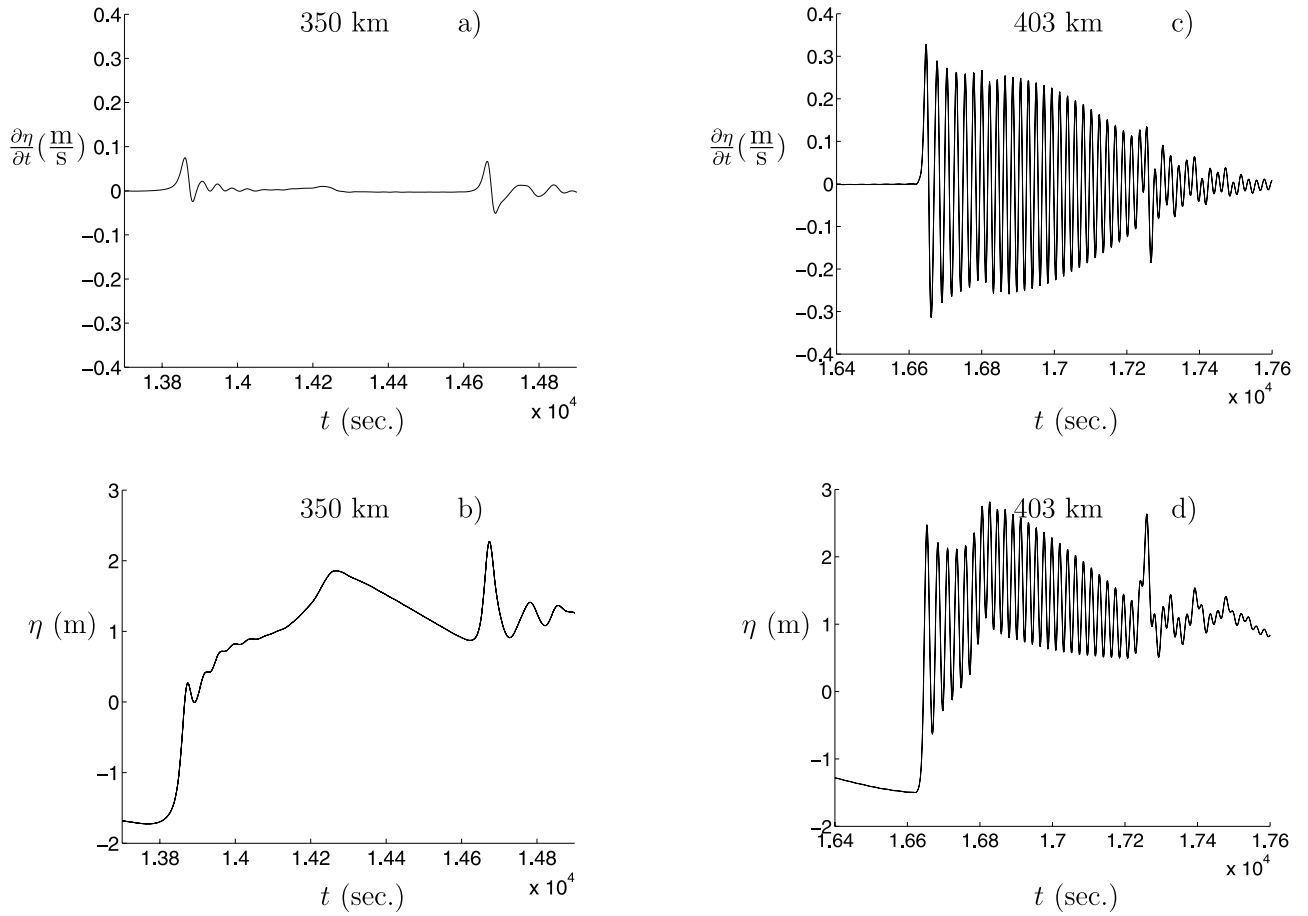

Figure 8. Time series of elevation η (in meters) and its time derivative $\partial\eta/\partial t$ (in m/s) at positions 350 and 403 km for full solution and half initial amplitude.

[46] The energy transfer in the FNDM and KdV is compared in Figure 10. At late stages (403 km) the KdV model significantly overpredicts the wave energy at high modes for both input waves (5.2 and 2.6 m). It is evident that the KdV equation has a limited capacity for resolving the dispersion effect when the train of short waves moves into deeper water behind the third bottom ridge.

[47] (We note that the vanishingly small effect of the short waves that are present in the input wave have no implications for the downshift as illustrated in Figures 9 and 10. The contrary would mean a significant portion of energy in $|\mathcal{F}_0(\eta_t)|$ at 0 km.)

3.8. Comparison to the Undular Bores Computed by *Glimsdal et al.* [2006]

[48] *Glimsdal et al.* [2006] used the Boussinesq equations to calculate the wave motion in the Strait of Malacca along a section S S, marked in Figure 1a, that intersects with the shoreline north of the end point B of our simulations. Their simulations exhibited an undular bore with a wavelength of 500 m in water depth of 15 m between 2 and 7 km from the shoreline, corresponding to a wave period of 41 s and short-wave height of about 5 m for their strongest source and less than 1 m for another, weaker source [*Glimsdal et al.*, 2006, Figure 17]. Our simulations with the 5.2 m high input wave show an elevation that runs between −3 and +3 m at the station at 250 km, twice as large as given by Glimsdal et al., and that the train of short waves is present in its initial phase, unlike in the work of Glimsdal et al. Our simulations with the 2.6 m input wave give a wave height of 3 m and a maximal wave slope of 0.35×10^{-3} at 250 km, and this input wave is relatively close to the wave caused by the weaker source as in the work of Glimsdal et al.

[49] Glimsdal et al. compared their global predictions of the Indian Ocean tsunami to the observations at the yacht *Mercator*. While an overall good agreement with the total wave height was found, the local wave slope was much smaller in computation ($\eta_t \simeq 0.004$ m/s and $\eta_x = 0.32 \times 10^{-3}$ at maximum) than in observation ($\eta_t \simeq 0.024$ m/s and $\eta_x = 2.2 \times 10^{-3}$ at maximum). One may speculate that the waves computed by Glimsdal et al. were less steep than the real waves that occurred in the Indian Ocean tsunami.

4. Summary and Conclusions

[50] We present model simulations of how the back face of a long leading depression wave moving into the shallow Strait of Malacca may develop into an undular bore and may split up into a number of solitary waves. The wave motion has been studied along a 420 km long section that is midway in the strait. The bottom topography has an initial depth of 156 m and three subsequent subsea ridges, with local depths of 70, 65, and 36 m at distances of 206, 300, and 375 km, respectively, from the initial point.

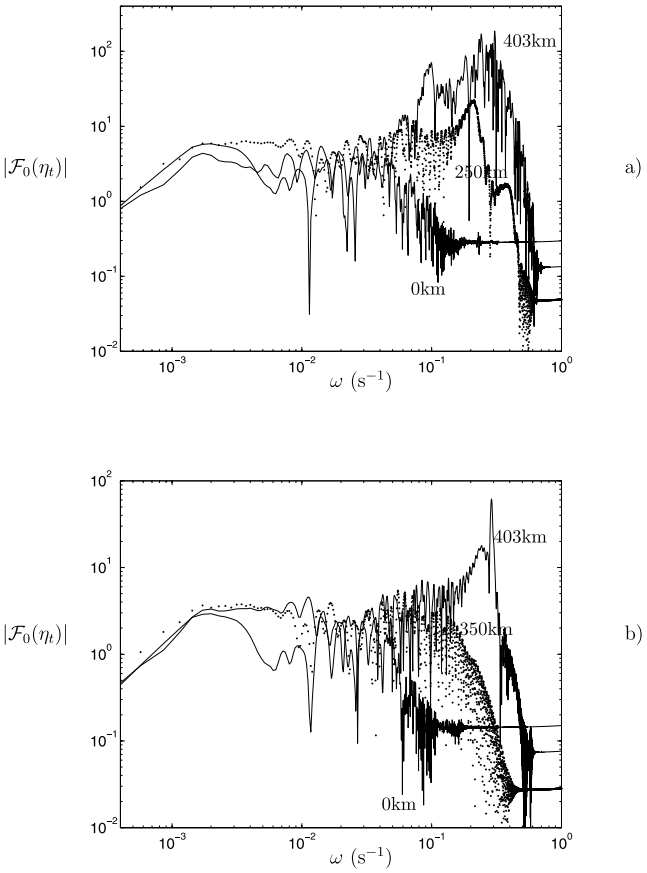

Figure 9. Upshift of energy by fully nonlinear dispersive computations: $|\mathcal{F}_0(\eta_t)|$ versus ω at (a) 0 (initial), 250, and 403 km using the original incoming wave and (b) 0 (initial), 350, and 403 km using half amplitude of original incoming wave.

[51] The simulations assume an initial waveform at the entrance of the strait as predicted by the TUNAMI code (see section 1), with initial water displacement in the source determined using seismological models, for the 26 December 2004 Indian Ocean tsunami. The initial wave has a leading depression and subsequent elevation. The total period is about 4500 s, length is about 176 km, and height is 5.2 m. The trough to crest period of the back face of the wave is about 1000 s, however, corresponding to 17 min, and is where the short waves develop. The wave height of 5.2 m corresponds to observations at a yacht located somewhat north of our starting point of the simulation; see video of tsunami observations by the echo sounder on yacht *Mercator*, Phuket (available at http://www.knmi.nl/VinkCMS/news_detail.jsp?id=19222). For comparison, we have also propagated a wave along the section with half initial amplitude.

[52] The 5.2 m tall input wave has an initial maximal wave slope of 0.02×10^{-3}, and the 2.6 m tall wave has an initial maximal wave slope of 0.01×10^{-3}. The leading depression wave undergoes a significant steepening in its back face during the motion, and short waves emerge when the wave slope becomes 0.0036–0.0038 for both input waves. The dominant period of the short waves attains a value slightly longer than 20 s in the end of the section for both input waves and illustrates the fundamental role of the bottom topography in the transformation process of the long incoming wave. The formation of short waves means that there is a significant transfer of energy from long to short modes. The short-wave group develops earlier for the 5.2 m input wave, at the first subsea peak at 200 km, than for the 2.6 m input wave at the third subsea peak at 350 km. The short waves develop into a train of rank-ordered solitary waves moving faster than the leading long depression wave. Similar generation of short waves occurs for tidally driven interfacial motion at sills in the layered ocean, where the short waves in an initial phase satisfy the linear dispersion relation for interfacial flow, growing then in amplitude, subsequently forming interfacial solitary waves of large amplitude as observed in fully nonlinear interfacial computations [*Grue*, 2005, 2006].

[53] Providing motivation for the study, video recordings of undular bores in the Strait of Malacca, although not of good quality, indeed indicate a short-wave period in the range of 15–20 s at the beach, close to the dominant short-wave period observed in the present simulations (see http://www.dagbladet.no/download/malaysia_wave.wmv).

[54] The train of short waves draws energy from the steep back of the leading depression wave. In the beginning, the

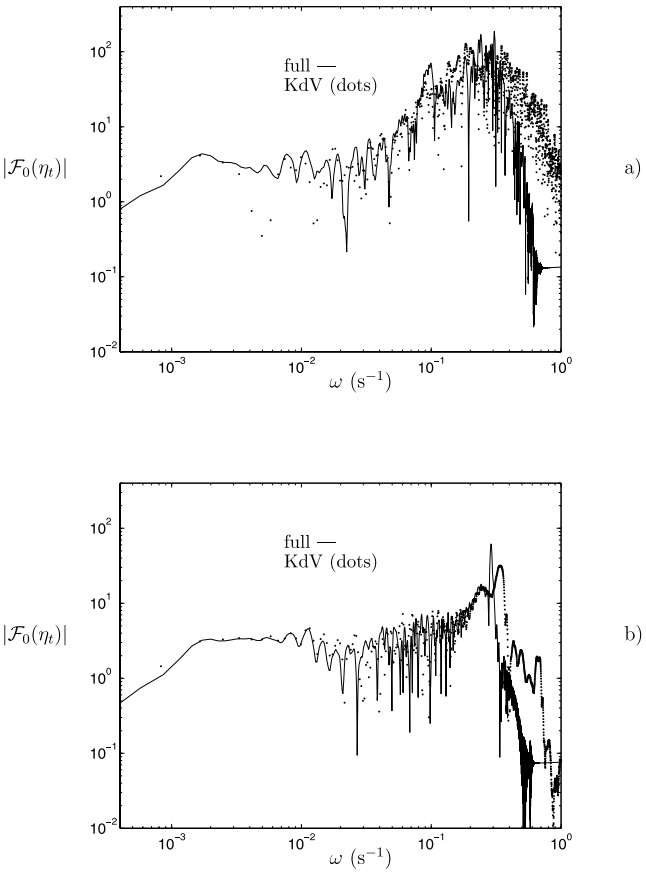

Figure 10. Upshift of energy at 403 km for fully nonlinear dispersive model (solid line) and KdV (dots). (a) Initial wave as in Figure 2a, with wave height 5.2 m, and (b) initial wave with half amplitude (2.6 m).

group of short waves has very small amplitude and behaves like a linear dispersive wave train. While the steep front, where the short waves are born, propagates with the shallow water speed $\sqrt{gh}$, the tail of the train of short waves moves with the linear group velocity, $\partial\omega/\partial k$, where $\omega^2 = gk \tanh kh$. The train of short waves extends behind the steep front since $\sqrt{gh} > \partial\omega/\partial k$. The shortest waves modeled here have kh up to about 0.7 (for both input waves) and maximal wave height to depth ratio up to about 0.4 (for the 5.2 m tall input wave), indicating that the motion is outside the range of validity of weakly nonlinear dispersive theories.

[55] Careful examination of the short-wave formation exhibits properties of undular bores as documented in the classical studies by *Favre* [1935] (measurements) and *Peregrine* [1966] (computations). Undular bores are nonbreaking when $\Delta\eta/h < 0.28 - \Delta\eta$, when there is a change in water level, where h is water depth. At least one of the leading waves of the undular bore is breaking when $0.28 < \Delta\eta/h < 0.75$ [*Binnie and Orkney*, 1955]. For greater differences in depth there are no short waves. In our simulations $\Delta\eta/h = 0.074$ for the 5.2 m input wave and 0.06 for the 2.6 m input wave, where the short waves emerge, so the short waves observed here fall into the category of nonbreaking undular bores. The short waves emerge when the slope of the main wave reaches a value of 0.0036–0.0038, as mentioned. Slope of the short waves reaches a maximum of 0.0667, corresponding well to the maximum slope of the undular bore computed by *Peregrine* [1966] in his strongest example. While kh of the short waves is up to about 0.7 here, Peregrine's computations based on the KdV equation exhibited kh up to unity, which is outside the range of validity of the KdV equation. Although maximum values of $\partial\eta/\partial t/\sqrt{gh}$ are similar in our and Peregrine's computations, the value of $\Delta\eta/h$ is much smaller here (0.074) than in his computations (up to 0.2). Consequently, the undulations have relatively higher amplitude here. *Keulegan and Patterson* [1940] employed KdV theory to show that the undulations measured by Favre had properties close to cnoidal waves, with formation of solitary waves in the long-wavelength limit. The formation of short waves developing eventually into a train of solitary waves implies a fission of the mother wave.

[56] Two models have been used in the computations including a fully nonlinear dispersive method (FNDM) and a variant of the Korteweg-de Vries (KdV) equation. The KdV model exhibits short waves of somewhat smaller amplitude in their generation phase than in the FNDM. At locations where kh becomes up to about 0.7, and the nonlinearity parameter, η/h, becomes up to about 0.4, the KdV model predicts unrealistically large wave peaks. After a propagation of 403 km the leading waves appear as solitary waves and are similar in the two models, except that the KdV method somewhat exaggerates the wave height and crest to crest separation. KdV, moreover, predicts a wider wave spectrum than the FNDM. The same conclusion applies when the amplitude of the input wave is divided by two: the KdV equation poorly resolves the short waves that become generated at the third ridge, particularly when the water depth increases behind the ridge.

[57] Despite the relatively good comparison between the FNDM and KdV for many of the features observed in the present calculations of undular bore, e.g., comparison to the classical KdV computations by *Peregrine* [1966] and to the relatively similar behavior in the KdV and FNDM at the onset of the short wave motion and in the final part of the propagation, it is evident that KdV has severe shortcomings compared to FNDM. This is exemplified in the calculations of the spectrum where KdV poorly resolves the motion at high wave numbers. An immediate recommendation is to choose a method that resolves short-wave motion well beyond $kh = 1$. With regard to nonlinearity this is very mild in the present computations at least at the onset of the short-wave formation. When the waves are grown up and the water gets very shallow, like at the shallowest ridge, the leading solitary waves have an amplitude to depth ratio up to 0.4 and are well outside the range of weakly nonlinear models. The Ursell number was up to a value of 3 at 350 km, for example, indicating a very strong effect of nonlinearity. However, another important point is that an accurate representation of both nonlinearity and dispersion is required for an accurate modeling of the evolution of nonlinear dispersive wavefields over long distance and time. Small misrepresentation of nonlinearity and dispersion therefore leads to erroneous results. Finally, in the present computations with then FNDM we used resolutions of $\Delta x = 40$ m and 20 m, both giving the same result. Coarser resolutions were tested but found insufficient.

[58] **Acknowledgments.** J.G. and D.F. were funded by the Reserach Council of Norway through the Strategic University Program, "Modeling of currents and waves for sea structures," at the University of Oslo (NFR 146526/420); E.N.P., T.T., and C.K. were funded by INTAS (06-1000013-9236), RFBR (05-05-64265), and a grant ARCUS.

References

Bateman, W. J. D., C. Swan, and P. H. Taylor (2001), On efficient numerical simulation of directionally spread surface water waves, *J. Comput. Phys.*, *174*, 277–305.

Berezin, Y. A. (1987), *Modelling Nonlinear Wave Processes*, VNU Sci., Utrecht, Netherlands.

Binnie, J. A. M., and C. Orkney (1955), Experiments on the flow of water from a reservoir through an open channel. II: The formation of hydraulic jumps, *Proc. R. Soc. London, Ser. A*, *230*, 237–246.

Caputo, J.-G., and Y. A. Stepanyants (2003), Bore formation, evolution and disintegration into solitons in shallow inhomogeneous channels, *Nonlinear Processes Geophys.*, *10*, 40–424.

Clamond, D., and J. Grue (2001), A fast method for fully nonlinear water wave computations, *J. Fluid Mech.*, *447*, 337–355.

Clamond, D., D. Fructus, and J. Grue (2007), A note on time integrators in water-wave simulations, *J. Eng. Math.*, *58*, 149–156.

Dalrymple, R. A., S. T. Grilli, and J. T. Kirby (2006), Tsunamis and challenges for accurate modeling, *Oceanography*, *19*(1), 142–151.

Didenkulova, I. I., N. Zahibo, A. A. Kurkin, B. V. Levin, E. N. Pelinovsky, and T. Soomere (2006), Runup of nonlinearly deformed waves on a coast, *Dokl. Earth Sci.*, *411*(8), 1241–1243.

Favre, H. (1935), *Ondes de Translation*, 4th ed., Dunod, Paris.

Fructus, D., and J. Grue (2007), An explicit method for the nonlinear interaction between water waves and variable and moving bottom topography, *J. Comput. Phys.*, *222*, 720–739.

Fructus, D., D. Clamond, J. Grue, and Ø. Kristiansen (2005), An efficient model for three-dimensional surface wave simulations, part I: Free space problems, *J. Comput. Phys.*, *205*, 665–685.

Glimsdal, S., G. K. Pedersen, K. Atakan, C. B. Harbitz, H. P. Langtangen, and F. Løvholt (2006), Propagation of the Dec. 26, 2004, Indian Ocean tsunami: Effects of dispersion and source characteristics, *Int. J. Fluid Mech. Res.*, *33*(1), 15–43.

Gonzales, F. I., and Y. A. Kulikov (1993), Tsunami dispersion observed in the deep ocean, in *Tsunamis in the World*, pp. 7–16, Kluwer Acad., Dordrecht, Netherlands.

Grue, J. (2002), On four highly nonlinear phenomena in wave theory and marine hydrodynamics, *Appl. Ocean Res.*, *24*, 261–274.

Grue, J. (2005), Generation, propagation and breaking of internal solitary waves, *Chaos*, *15*, 037110, doi:10.1063/1.2047907.

Grue, J. (2006), Very large internal waves in the ocean—Observations and nonlinear models, in *Waves in Geophysical Fluids: Tsunamis, Rogue Waves, Internal Waves and Internal Tides, CISM Courses Lect. Ser.*, vol. 489, edited by J. Grue and K. Trulsen, pp. 205–270, Springer, New York.

Hammack, J. (1973), A note on tsunamis: Their generation and propagation in an ocean of uniform depth, *J. Fluid Mech.*, *60*, 769–799.

Horrillo, J., Z. Kowalik, and Y. Shigihara (2006), Wave dispersion study in the Indian Ocean tsunami of December 26, 2004, *Sci. Tsunami Hazards*, *25*(1), 42–63.

Intergovernmental Oceonographic Commission (1997), IUGG/IOC Time Project: Numerical method of tsunami simulation with the leap-frog scheme, *IOC Manuals Guides 35*, UNESCO, Paris.

Ioualalen, M., E. N. Pelinovsky, J. Asavanant, R. Lipikorn, and A. Deschamps (2007), On the weak impact of the 26 December Indian Ocean tsunami on the Bangladesh coast, *Nat. Hazards Earth Syst. Sci.*, *7*, 141–147.

Johnson, R. S. (1972), Some numerical solutions of a variable-coefficient Korteweg-de Vries equations (with applications to soliton wave development on a shelf), *J. Fluid Mech.*, *54*, 81–91.

Johnson, R. S. (1997), *A Modern Introduction to the Mathematical Theory of Water Waves*, Cambridge Univ. Press, New York.

Kanoglu, U., and C. Synolakis (2006), Initial value problem solution of nonlinear shallow water-wave equations, *Phys. Rev. Lett.*, *97*, doi:10.1103/PhysRevLett.97.148501.

Keulegan, G. H., and G. W. Patterson (1940), Mathematical theory of irrotational translation waves, *J. Res. Natl. Bur. Stand. U.S.*, *24*, 47–101.

Kulikov, E. A., and F. Gonzales (1995), Reconstruction of tsunami shape in the source based on measurements of hydrostatic pressure by bottom station (in Russian), *Dokl. Earth Sci.*, *344*(6), 814–818.

Liu, P. L.-F. (2005), Tsunami simulations and numerical models, *Bridge*, *35*(2), 14–20.

Liu, P. L.-F., H. Yeh, and E. A. Synolakis (Eds.) (2008), Advanced numerical models for simulating tsunami waves and runup, in *Advances in Coastal and Ocean Engineering*, World Sci., N. J. Hackensack, in press.

Lynett, P., and P. L.-F. Liu (2002), A numerical study of submarine-landslide generated waves and runup, *Proc. R. Soc. London, Ser. A*, *458*, 2885–2910.

Madsen, P. A., H. B. Bingham, and H. Liu (2002), A new Boussinesq method for fully nonlinear waves from shallow to deep water, *J. Fluid Mech.*, *462*, 1–30.

Mei, C. C. (1989), *The Applied Dynamics of Ocean Surface Waves*, 740 pp., World Sci., Hackensack, N. J.

Mirchina, N. R., and E. N. Pelinovsky (1982), Nonlinear and dispersive effects for tsunami waves in the open ocean, *Int. J. Tsunami Soc.*, *1*, D1–D9.

Mirchina, N. R., and E. N. Pelinovsky (1984), Solitons in the tsunami problem, in *Nonlinear and Turbulent Processes in Physics*, 2nd ed., edited by R. Sagdeev, pp. 973–978, Routledge, Boca Raton, Fla.

Murty, T. (1977), *Seismic Sea Waves: Tsunamis*, Bull. Fish. Res. Board Can., 198, 337 pp.

Ostrovsky, L. A., and E. N. Pelinovsky (1970), Wave transformation on the surface of fluid of variable depth, Izvestiya, *Atmos. Ocean Phys.*, *6*, 552–555.

Pelinovsky, E. N. (1996), *Hydrodynamics of Tsunami Waves* (in Russian), Appl. Phys. Inst., Nizhny Novgorod, Russia.

Pelinovsky, E. N. (2006), Hydrodynamics of tsunami waves, in *Waves in Geophysical Fluids: Tsunamis, Rogue Waves, Internal Waves and Internal Tides*, *CISM Courses Lect. Ser.*, vol. 489, edited by J. Grue and K. Trulsen, pp. 1–48, Springer, New York.

Pelinovsky, E. N., T. Talipova, A. Kurkin, A. Kozelkov, and N. Zahibo (2005), Nonlinear and dispersion effects in the tsunami wave field, paper presented at 22nd International Tsunami Symposium, Inst. of Geodyn., Natl. Obs. of Athens, Chania, Greece, 27–29 June.

Peregrine, D. H. (1966), Calculations of the development of an undular bore, *J. Fluid Mech.*, *25*, 321–330.

Rivera, P. C. (2006), Modeling the Asian tsunami evolution and propagation with a new generation mechanism and a non-linear dispersive wave model, *Sci. Tsunami Hazards*, *25*(1), 18–33.

Satake, K. (1995), Linear and nonlinear computations of the 1992 Nicaragua earthquake tsunami, *Pure Appl. Geophys.*, *144*, 455–470.

Shuto, N. (1985), The Hihonkai-Chubu earthquake tsunami on the north Akita coast, *Coastal Eng. Jap.*, *28*, 255–264.

Voit, S. S. (1987), Tsunamis, *Annu. Rev. Fluid Mech*, *19*, 217–236.

Yalciner, A. C., , E. N. Pelinovsky, E. Okal, and C. E. Synolakiks (Eds.) (2003), *Submarine Landslides and Tsunamis*, *NATO Sci. Ser., Ser. IV*, vol. 21, Springer, New York.

Zaitsev, A. I., A. A. Kurkin, B. V. Levin, E. N. Pelinovsky, A. Yalciner, Y. I. Troitskaya, and S. A. Ermakov (2005), Numerical simulation of catastrophic tsunami propagation in the Indian Ocean, *Dokl. Earth Sci.*, *402*(4), 614–618.

D. Fructus and J. Grue, Mechanics Division, Department of Mathematics, University of Oslo, P. O. Box 1053 Blindern, NO-0316 Oslo, Norway. (johng@math.uio.no)

C. Kharif, Institute de Recherche sur les Phénomènes Hors Equilibre, Technopole de Chateau-Gombert, 49 Rue Frederic Joliot-Curie, B. P. 146, F-13384 Marseille Cedex 13, France.

E. N. Pelinovsky and T. Talipova, Department of Nonlinear Geophysical Processes, Institute of Applied Physics, 46 Uljanov Street, 603950, GSP-120, Nizhny Novgorod, Russia.